The Influence of Whitecapping Waves on the Vertical Structure of Turbulence in a Shallow Estuarine Embayment

NICOLE L. JONES* AND STEPHEN G. MONISMITH

Environmental Fluid Mechanics Laboratory, Civil and Environmental Engineering, Stanford University, Stanford, California

(Manuscript received 25 January 2007, in final form 6 December 2007)

ABSTRACT

The vertical distribution of the turbulent kinetic energy dissipation rate was measured using an array of four acoustic Doppler velocimeters in the shallow embayment of Grizzly Bay, San Francisco Bay, California. Owing to the combination of wind and tide forcing in this shallow system, the surface and bottom boundary layers overlapped. Whitecapping waves were generated for a significant spectral peak steepness greater than 0.05 or above a wind speed of 3 m s^{-1}. Under conditions of whitecapping waves, the turbulent kinetic energy dissipation rate in the upper portion of the water column was greatly enhanced, relative to the predictions of wind stress wall-layer theory. Instead, the dissipation followed a modified deep-water breaking-wave scaling. Near the bed (bottom 10% of the water column), the dissipation measurements were either equal to or less than that predicted by wall-layer theory. Stratification due to concentration gradients in suspended sediment was identified as the likely cause for these periods of production–dissipation imbalance close to the bed. During 50% of the well-mixed conditions experienced in the month-long experiment, whitecapping waves provided the dominant source of turbulent kinetic energy over 90% or more of the water column.

1. Introduction

In recent years, many studies have been directed toward understanding the physical processes that determine mixing in the surface boundary layer. These studies are motivated by the important role of the surface boundary layer in the transfer of heat, gas, and momentum from the atmosphere, which is fundamental to the physical and biogeochemical processes in water bodies such as oceans, lakes, and reservoirs (Thorpe 2004). At the water surface, momentum is transferred from the wind to the water column. A surface wind stress can create a wall layer extending from the air–water interface downward, analogous to the bottom boundary layer (Gargett 1989). However, the wind also creates surface waves, which enhance the turbulent kinetic energy (TKE) near the surface via processes such as wave breaking, which in turn enhance the transfer of momentum to the surface current field (Terray et al. 1996, hereafter TEA96).

Surface waves have the potential to modify the hydrodynamics near the free surface in three ways (Craig and Banner 1994). First, the interaction of the wave Stokes drift with the wind-driven surface shear current can result in Langmuir circulation formation (e.g., Craik and Leibovich 1976; Skyllingstad and Denbo 1995; Teixeira and Belcher 2002). Second, Reynolds stresses can be created when the waves are not perfectly irrotational (e.g., Magnaudet and Thais 1995). Third, breaking waves generate TKE that is available to be mixed down into the surface layer (Agrawal et al. 1992; TEA96); this mechanism was the focus of this study.

TKE dynamics is often quantified by measuring the TKE dissipation rate ε. Measurements of ε by stationary (Agrawal et al. 1992; TEA96), shipborne (Drennan et al. 1996, hereafter DDTK96) wave-following (Soloviev and Lukas 2003; Gemmrich and Farmer 2004), and profiling instruments (Anis and Moum 1995; Greenan et al. 2001; Stips et al. 2005) have

* Current affiliation: School of Environmental Systems Engineering, The University of Western Australia, Crawley, Western Australia, Australia.

Corresponding author address: Nicole L. Jones, School of Environmental Systems Engineering, The University of Western Australia, MO15, 35 Stirling Highway, Crawley, WA 6009, Australia.
E-mail: nicole.jones@uwa.edu.au

DOI: 10.1175/2007JPO3766.1

shown that deep water breaking waves lead to levels of ε that are elevated above those predicted by wall-layer theory. The TEA96 model of the wave-affected surface layer (WASL) divides the WASL into two sublayers. The two-layer model assumes that, adjacent to the surface water, direct injection of TKE by wave breaking occurs, leading to near-constant ε rates and negligible rates of shear production (TEA96). This layer is termed the wave breaking sublayer. The second layer is termed the transition sublayer. Here the vertical transport of TKE exceeds the shear production of TKE (e.g., TEA96). TEA96 collapsed their near-surface ε measurements using the estimated wind energy input F, the significant wave height H_s, and the depth below the water surface z':

$$\frac{\varepsilon H_s}{F} = c\left(\frac{z'}{H_s}\right)^{-b}. \tag{1}$$

This relationship, with $c = 0.3$ and $b = 2$, has been shown to hold for both young (TEA96) and more developed seas (DDTK96). Terray et al. (1999) combined the observations of Anis and Moum (1995), TEA96 and DDTK96 and found that $b = 2.3 \pm 0.4$. However, the Gargett (1989) near-surface ε dataset revealed a z'^{-4} depth dependence. Greenan et al. (2001) found that the TEA96 Water Air Vertical Exchange Studies (WAVES) scaling held for windsea conditions; however, they found that for more complex open ocean conditions, where windsea and swell interact, the relationship of $\varepsilon \propto z'^{-1}$ was better suited than $\varepsilon \propto z'^{-2}$.

Below the WASL, ε has been shown to scale with the predictions of wall-layer theory owing to the surface wind stress u_{*w} (Agrawal et al. 1992; Monismith and Magnaudet 1998); that is,

$$\varepsilon = \frac{u_{*w}^3}{\kappa z'}, \tag{2}$$

where $\kappa = 0.41$ is the von Kármán constant. The transition between the WASL and the wind stress log-layer occurs at the depth where shear production of turbulence dominates the transport of TKE due to wave breaking.

Near the bed, turbulence is generated by the vertical shear of the mean flow at the sediment–water interface. Many studies have shown that shear production and ε are in balance in the bottom boundary layer (e.g., Gross and Nowell 1985; Reidenbach et al. 2006) such that ε scales as

$$\varepsilon = \frac{u_{*b}^3}{\kappa z}, \tag{3}$$

where u_{*b} is the bed stress and z is the height above the bed ($z = h - z'$, where h is the water depth).

In shallow water bodies, such as estuarine embayments and shoals, shallow lakes, and the nearshore region along a coast, the surface and bottom boundary layers may overlap. Strong winds can produce whitecapping waves in these water bodies while the tide-driven pressure gradients and the surface wind stress drive the mean flow (Bricker et al. 2005). Recent measurements of ε in the nearshore zone suggest that in the surface layer the deep water wave breaking scaling of TEA96 applies (Feddersen et al. 2007). However, at their nearshore measurement location, the negligible vertical shear in the mean current leads to values of shear production that are much smaller than ε at all depths. Preliminary analysis of ε measurements under whitecapping waves in a shallow lake (~2 m deep) also indicates that ε often exceeds the law-of-the-wall scaling (Young et al. 2005). To the authors' knowledge, at present no studies have investigated the influence of whitecapping waves on the vertical distribution of TKE in a shallow, tide-forced environment.

Many shallow estuaries in the world, in particular those formed by drowned river valleys, comprise one or more deep channels laterally bounded by broad shallow regions (<4 m) (Conomos et al. 1985; Thompson et al. 2008). San Francisco Bay is an example of an estuary with this type of bathymetry (Fig. 1). Substantial fetches O(5–10 km) in these shallow water bodies lead to the production of short period waves (~2 s), exceeding 0.5 m in height under strong wind conditions (wind speed at 10 m, $U_{10} \sim 12$ m s^{-1}), which whitecap owing to depth-limited breaking and wave steepening (Babanin et al. 2001). This tide-forced estuarine environment can lead to the formation of a strongly sheared bottom boundary layer; therefore shear production is also likely to be an important source of TKE to the water column. Understanding the dynamics of the shallow embayments and shoals of estuaries is critical to the prediction of sediment transport and biological processes, such as the distribution of phytoplankton.

The purpose of this study is to quantify the influence of whitecapping waves on the vertical distribution of turbulence in a shallow estuarine embayment, where the surface wind/wave-driven boundary layer overlaps with the tide-forced bottom boundary layer. Observations of the vertical structure of ε, mean currents, and temperature were made in a shallow embayment in San Francisco Bay. Comparison of ε with the bed log-layer scaling revealed the probable occurrence of suspended sediment stratification close to the bed (section 4a). Comparison of the observations with the wind-driven surface boundary layer scaling was inconclusive (section 4b); however, the deep water wave breaking

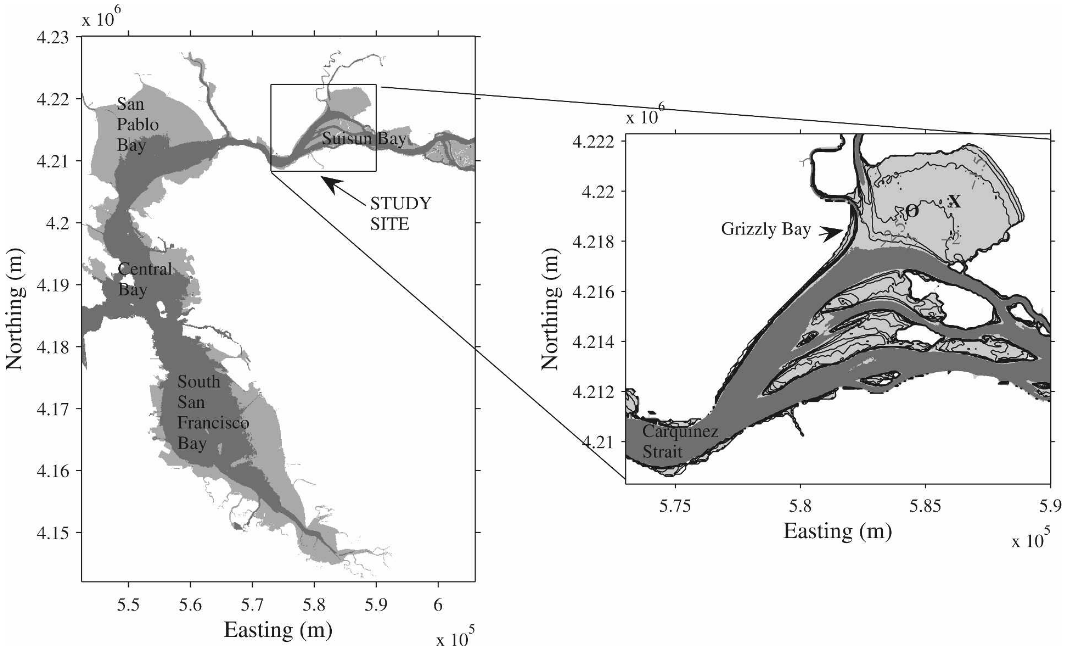

FIG. 1. Bathymetric contours and site map of Suisun Bay showing the location of the ADV frame (cross) and the wind anemometer and camera platform (open circle). The darker gray areas indicate depth greater than 4 m.

scaling of TEA96 was found to collapse the ε measurements in the surface layer under conditions of whitecapping waves (section 4c). The initiation of whitecapping as a function of wave age, wind speed, and significant spectral peak steepness was explored using hourly photographs of the field site (section 5). In the absence of stratification, whitecapping waves provided the dominant source of TKE over 90% or more of the water column for half of the monthlong period (section 7).

2. Experimental methods and conditions

a. Study site

The measurements were made in Grizzly Bay, San Francisco Bay, California (Fig. 1), from 1 May to 2 June 2005. Grizzly Bay is a subembayment of Suisun Bay. It covers approximately 24 km^2 and has a mean depth of 1.25 m [defined as the volume at mean lower low water divided by the surface area; Warner et al. (2004)]. The bathymetry is typical of a bay in that the contours follow the curved shape of the shoreline. The tides are semidiurnal with a range of approximately 2 m in this area.

During the measurement period the prevailing winds were generally from the southwest and west and displayed a diurnal pattern in strength. The predominant direction of the wind aligned with the longest fetch, a distance of roughly 13 km, producing relatively large wind waves in Grizzly Bay.

b. Instrument deployment

The experiment site was located approximately in the center of the embayment (Fig. 1). An array of four acoustic Doppler velocimeters (ADVs) (Vector, Nortek AS) recorded velocity and pressure at four heights above the bed (0.15, 0.5, 1.5, and 2 m) in a water column of mean depth 2.5 m. These were synchronized with a capacitance wave height gauge (WG50, RBR) (Fig. 2). The ADVs and capacitance wave gauge were sampled for a period of 10 min at 16 Hz every 30 min. A vertical array of five thermistors (SBE39, Seabird Electronics) and two conductivity sensors (SBE16+, Seabird Electronics) were used to identify periods of stratification. Vertical profiles of the mean velocity (with 10-cm spatial resolution) were measured with a Doppler current profiler (Aquadopp Profiler, Nortek AS). A wind anemometer (wind monitor model 05103, R. M. Young Company), situated approximately 6 m above mean water level, recorded wind velocity statistics every 10 min, including average wind speed and direction. A record of "sea state" was gained via a high-resolution camera, located on the wind anemometer platform, which recorded five images hourly during daylight (Fig. 3).

c. Analysis

The 10-m wind speed and wind stress were estimated from the measured wind velocity via the Donelan (1990) algorithm, which was developed for fetch-

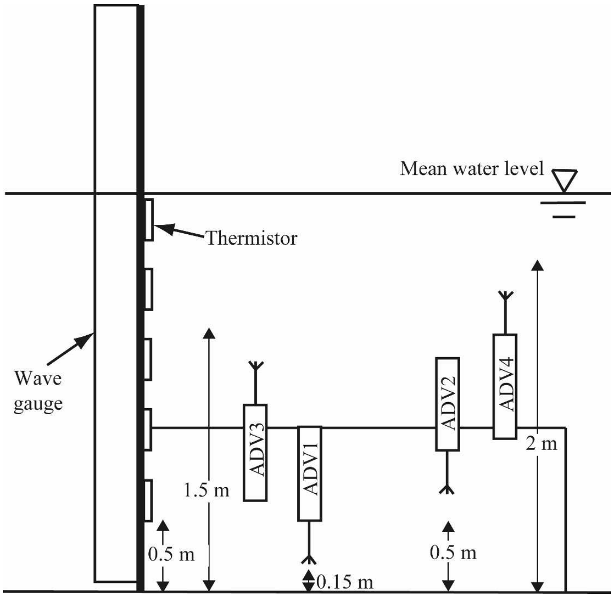

FIG. 2. Schematic of ADV frame. Heights of ADVs indicate location of measurement volume relative to the bed.

FIG. 3. Photograph of the retired navigation structure used to mount the wind anemometer and digital camera.

limited lakes and accounts for the effect of waves and whitecapping on the wind stress. Wave height and period were calculated from the pressure records of the ADVs as the capacitance wave gauge was destroyed three days into the experiment. The short wave gauge record was used to optimize the analysis method for estimating wave properties from the pressure measurements (Jones and Monismith 2007). Linear wave theory was used to convert the pressure spectra to surface elevation spectra and the spectra were extrapolated in the equilibrium range, with an f^{-4} slope beyond the identified frequency where the signal-to-noise ratio of the pressure signal was too low. Using the method described in Jones and Monismith (2007), H_s can be estimated from the pressure records with an uncertainty of 0.034 m at a 95% confidence level.

Dissipation was calculated from the 10-min ADV records. We selected the 10-min sample period as a compromise between adequately sampling the wave field and minimizing changes in the mean tide and wind velocities. The resulting calculation of ε represents an average of the conditions experienced over each sample period as wave breaking is an intermittent process (Rapp and Melville 1990). Each 10-min ADV vertical velocity record was divided into 32 sections of equal length, each with 50% overlap. Each segment was windowed with a Hamming window, and the fast Fourier transform calculated. All 63 spectral estimates were ensemble averaged to produce a resultant spectral estimate with 188 degrees of freedom (Emery and Thomson 2001). An example spectrum is shown in Fig. 4. The expected spectral value is within a factor from 0.88 to 1.15 of the sample value at 90% confidence limits.

Dissipation was calculated from a $-5/3$ fit to the inertial subrange of the vertical velocity spectra $S_{w'w'}$ for frequencies greater than the peak wave frequency, employing the Lumley and Terray (1983) model to account for the effects of waves on the turbulent wavenumber spectrum (Trowbridge and Elgar 2001; Feddersen et al. 2007). The method detailed in Feddersen et al. (2007) was used to estimate ε from the observed $S_{w'w}$ [defined such that $\int_0^\infty S_{w'w'}(\omega)d\omega$ = variance]. This method numerically evaluates the form of the TKE spectra for turbulence advected by both oscillatory and unidirectional velocities (Lumley and Terray 1983). The appendix details this method.

Since the broad wave peak was located within the inertial subrange, care was taken to verify the existence of an inertial subrange for each $S_{w'w'}$. We identified the location of the inertial subrange by searching for the sequence of points that resulted in the smallest least squares error for the $-5/3$ fit in log-space. The search was performed for frequencies greater than the peak wave frequency, and it was specified that the sequence of points had to span a minimum range of 2.5 Hz. Fol-

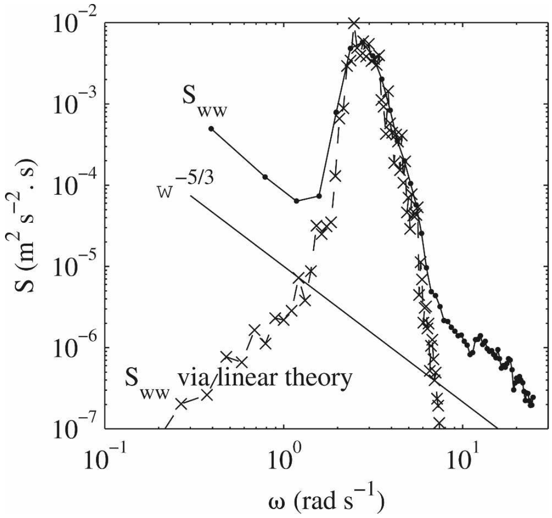

FIG. 4. Example of vertical velocity spectra with $\omega^{-5/3}$ region from ADV3, 0.9 m below the water surface, $H_s = 0.35$ m. Vertical velocity spectrum (solid line with circles) and vertical velocity spectrum predicted from the surface elevation measurements via linear wave theory (dashed line with crosses).

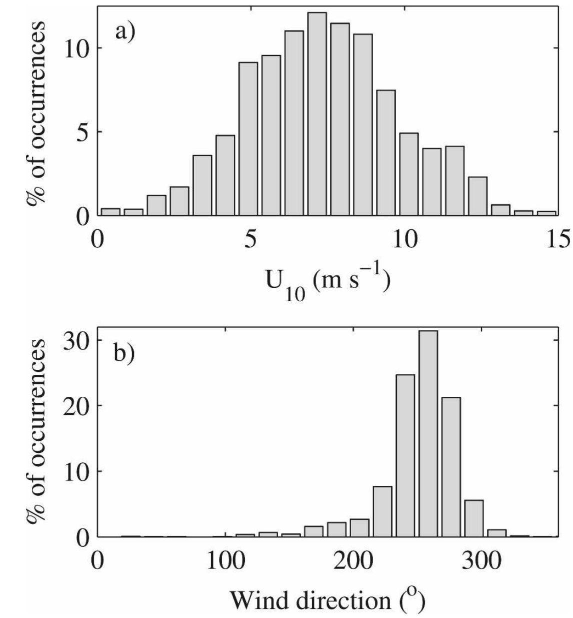

FIG. 5. Distribution of (a) wind speed U_{10} and (b) wind direction for the duration of the experiment. Wind direction is referenced to north, positive clockwise, and refers to the direction from which the wind is emanating.

lowing identification of the inertial subrange, we calculated ε using Eqs. (A1) and (A2) and $S_{w'w'}(\omega)$ from the $-5/3$ fit. The error in the ε estimate was calculated from the error in the intercept from the fit (90% confidence level) and propagated to the estimate of ε using a Monte Carlo approach (Emery and Thomson 2001); ε measurements with an error greater than the ε estimate itself were discarded. Using this method 3240 out of a total of 4458 measurements (or 73%) were deemed suitable for an estimate of ε.

Calculating the Reynolds stress from the ADV data in a wave–current environment requires the use of a wave–turbulence decomposition method, as the variance associated with the waves is often much larger than that associated with the turbulence. We used the decomposition method where velocity measurements at two heights are compared; motions that correlate between the sensors are identified as waves, while motions that are uncorrelated are defined as turbulence (Trowbridge 1998; Shaw and Trowbridge 2001; Feddersen and Williams 2007). The wave decomposition technique did not successfully remove wave contamination from the ADVs in the upper water column. Feddersen and Williams (2007) noted a similar problem in their nearshore measurements. Therefore, reliable measurements of Reynolds stress are only available 0.15 m above the bed (ADV1).

d. Wind, wave, and tide conditions

Distributions of the 10-min average wind speed (at 10 m) U_{10} and direction, measured for the duration of the experiment, are shown in Fig. 5. The most frequently observed wind speed was 7 m s^{-1}, although speeds up to 15 m s^{-1} were observed. The estimated wind stress in the direction of the major principal axis of the flooding current ranged from 0 to 0.4 $m^2 s^{-2}$ with a median value of 0.06 $m^2 s^{-2}$.

Locally generated waves with mean periods T_m varying from 1 to 1.6 s and H_s from 0 to 0.6 m were present during the experiment (Fig. 6). The experimental conditions resulted in predominantly intermediate depth windseas, as defined by linear wave theory, having a mean nondimensional depth $k_p h = 2.2$ (where k_p is the peak wavenumber). The wave age (peak wave phase speed normalized by the wind shear stress, c_p/u_{*a}) ranged from 6 to 15, which spans young to moderately developed waves. The dominant wave direction was estimated via the directional wave spectra using the extended maximum likelihood method (Isobe et al. 1984; Johnson 2002). Due to the bathymetry of the embayment, which refracts the waves toward the shoreline, the wave direction was predominantly toward the northeast for a range of wind directions. The photograph time series revealed a high occurrence of whitecapping waves at the site, often accompanied by the presence of windows.

Depth-averaged maximum currents at the measurement location were approximately -0.15 m s^{-1} on ebb and 0.25 m s^{-1} on flood (Figs. 7 and 8). The major

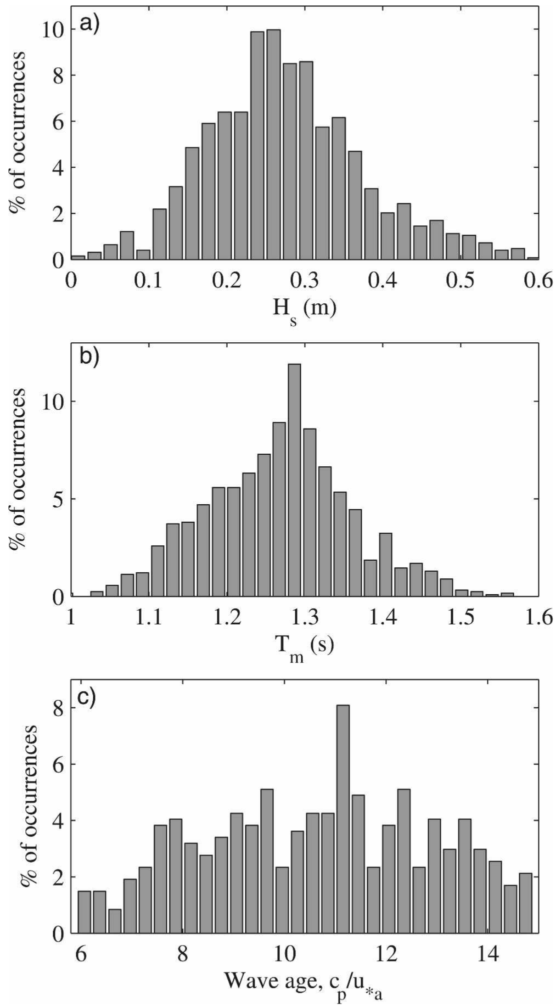

FIG. 6. Distributions of (a) significant wave height H_s, (b) mean wave period T_m, and (c) wave age c_p/u_{*a} for the duration of the experiment.

principal axis was 55°N. Therefore, we defined the coordinate system with u in the direction of the major principal axis (flood tide positive), v the minor axis, and w the vertical (positive upward) following a right-handed coordinate system. Comparison with the predominant wind direction reveals that the current was approximately directly opposing (following) the wind during ebb (flood) tides.

Weak wind-stress periods coincident with strong heat fluxes to the water column led to some periods of thermal stratification, which persisted for 2–6 h. In total, 14% of the observations were during stable stratification events (defined as periods when the gradient Richardson number, Ri > 0.25). Since the influence of whitecapping waves was the focus of this study, data collected when Ri > 0.25 (indicating stratification) or when the estimated buoyancy production was greater than 1×10^{-7} m^2 s^{-3} (indicating significant convective cooling) were removed from the analysis.

3. The vertical structure of dissipation

The typical vertical structure of ε measured under conditions of weak winds (<4 m s^{-1}) and strong winds (8–10 m s^{-1}) is shown in Figs. 9a and 9b, respectively. In these figures, we normalized the depth to take into account variation in water column height owing to the tide, and the magnitude of the depth-averaged velocity is distinguished by the color of the data point. Under weak wind conditions, when wave heights are very small, the magnitude of ε was approximately constant for a particular current magnitude over the bottom half of the water column (Fig. 9a). The values of ε increased with current magnitude, as expected. In the top half of the water column the pattern was less consistent; however, the majority of ε observations were less than 1×10^{-5} m^2 s^{-3}. Under stronger wind speeds ε was generally larger for the same current speed (Fig. 9b). In the upper 90% of the water column, the magnitude of ε was generally much higher than for weak wind speeds, with many observations exceeding 1×10^{-5} m^2 s^{-3}. Under strong wind conditions ε was up to three orders of magnitude larger at the surface than near the bed.

4. Scaling dissipation

a. Bed boundary layer scaling

If the influence of breaking waves on turbulence close to the bed is insignificant, then classic boundary-layer theory, which assumes that production and ε are in balance, should predict the magnitude of ε. Figure 10 illustrates that for the majority of measurements in the lower 10% of the water column $\varepsilon\kappa z/u_{*b}^3 < 1$, indicating that TKE injection due to wave breaking was not influencing these near-bed measurements. Higher in the water column, $\varepsilon\kappa z/u_{*b}^3 > 1$ for many of the observations, indicating that the wind stress and wave breaking were influencing ε.

The tendency for ε close to the bed to be smaller than predicted by bed boundary-layer (BBL) scaling (i.e., ε is smaller than shear production) indicates that the buoyancy production term may be less than zero; that is, the near-bottom water may be stably stratified. For ADV1 the mean value of $\varepsilon\kappa z/u_{*b}^3$ was 0.3. In general, minimal thermal and salinity gradients were present in the data; however, concentration gradients in suspended sediment near the bed may account for the disparity between the magnitude of ε and Eq. (3) (e.g., Cacchione et al. 1995; Green and McCave 1995). The

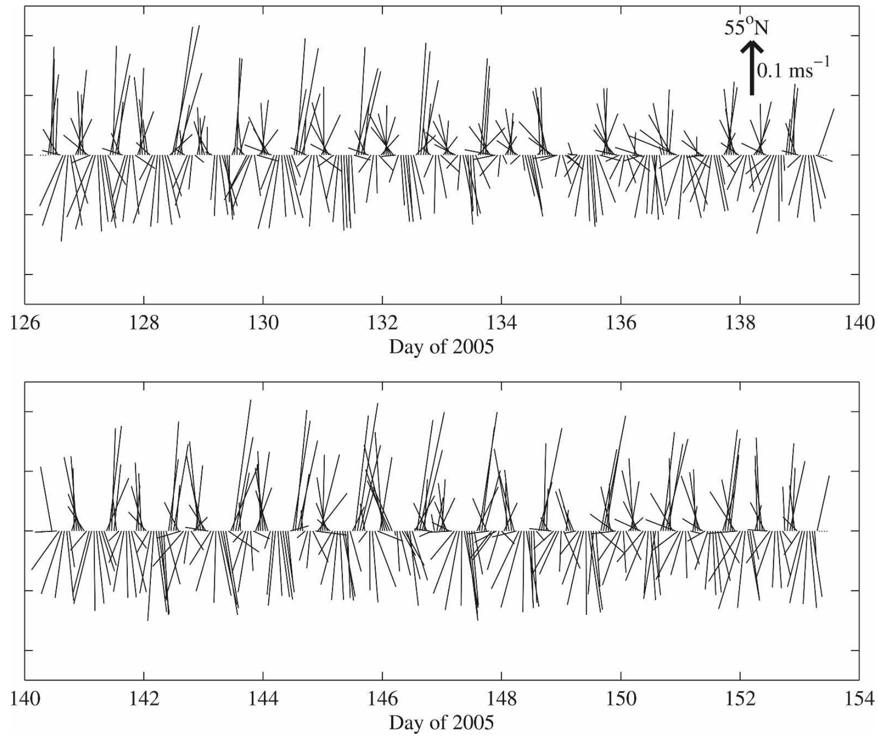

FIG. 7. Vector stick plots of the depth-averaged current at the field site for the month-long observation period.

Richardson number for suspended sediment describes the ratio of the stabilizing gravitational effects to the turbulence producing velocity shear; that is,

$$\mathrm{Ri} = \frac{w_s \kappa z g \mathrm{SSC}}{\rho u_{*b}^3}\left(1 - \frac{\rho}{\rho_s}\right), \tag{4}$$

where w_s is the settling velocity of the sediment particles, SSC is the mass concentration of the suspended sediment, ρ is the fluid density, and ρ_s is the sediment density (Cacchione et al. 1995). When $\mathrm{Ri} > 0.25$, turbulent shear is suppressed by the stabilizing effects of the stratification. However, studies have shown that the stratification begins to affect the turbulence at values as low as $\mathrm{Ri} = 0.03$ (e.g., Heathershaw 1979).

The SSC range corresponding to $0.03 < \mathrm{Ri} < 0.7$ can be estimated via Eq. (4) using observed values of $w_s = 5 \times 10^{-3}$ m s^{-1} and $\rho_s = 1077$ kg m^{-3} for San Francisco Bay flocculated sediment (Kranck and Milligan 1992). The SSC range was estimated to be $2 \times 10^{-2} < \mathrm{SSC} < 4 \times 10^{-1}$ kg m^{-3} for the average observed $u_{*b} = 5 \times 10^{-3}$ m s^{-1}. Warner et al. (2004) measured SSC in the range from 2×10^{-2} to 4.5×10^{-1} kg m^{-3} in the center of Grizzly Bay at a height of 0.3 m above the bed, indicating that sediment stratification is a plausible explanation for the observed imbalance between observed ε and ε predicted from BBL scaling.

b. Wind-driven surface boundary layer scaling

If the influence of breaking waves on near-surface turbulence is insignificant, then classic boundary-layer theory, which assumes that production and ε are in balance, should explain the magnitude of ε near the wind-shear-driven surface. When waves were present, the ADVs near the surface measured an enhanced ε rate close to the air–water interface relative to the predictions of wall-layer theory (Fig. 11). The depth below the surface is scaled with $u_{*w}{}^2/g$, which is proportional to the root-mean-square height of fully developed wind-forced waves (Agrawal et al. 1992).

The large range of nondimensional ε values for each nondimensional depth is due to the range of wave conditions experienced for each wind stress. The growth of the waves, and hence the extent of whitecapping, is a function of the longevity of the wind stress. It is difficult to conclude from Fig. 11 whether ε values begin to scale with the wall-layer values below the WASL, as some previous studies have shown (e.g., Agrawal et al. 1992). At greater depths ε begins to be dominated by the presence of the bed. A defined transition between the surface and bottom layer is not present in Fig. 11 as it varies with wind- and tide-forcing conditions. Furthermore, depending on the relative magnitude of the wind stress to the bed stress, measurements that scale

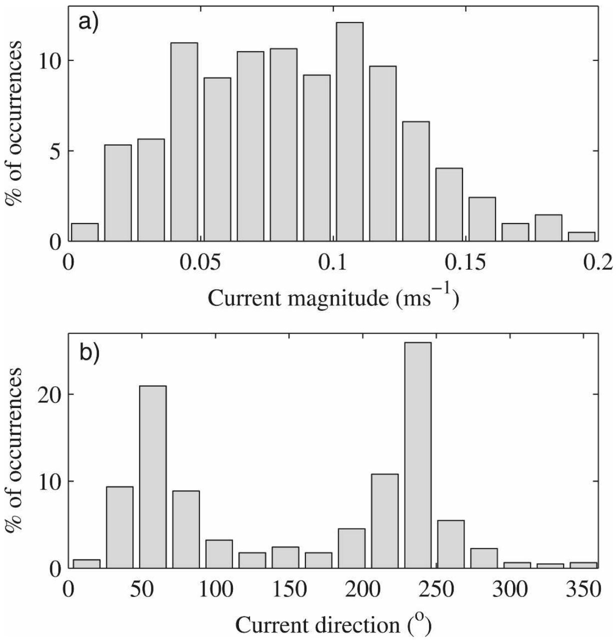

FIG. 8. Distribution of (a) depth-averaged current speed and (b) direction for the duration of the experiment. Current direction is referenced to north, positive clockwise, and refers to the direction of the current.

with the bed stress can be smaller or larger than $\varepsilon\kappa z'/u_{*w}^3 = 1$.

c. *Deep water wave breaking scaling*

TEA96 developed an alternative scaling of ε to account for the observations of enhanced ε in the surface transition layer [Eq. (1)]. The scaling is based on the assumption that wave breaking is the principal source of TKE in the near-surface layer and that breaking directly injects energy to depth z_b'. In the TEA96 model for the transition layer (i.e., where transport of TKE > production of TKE), ε is normalized by F/H_s, where F is the rate of energy input to the waves from the wind. The depth below the surface z' is normalized by H_s. Equation (1), with $b = 2$ and $c = 0.3$, was found to describe both the very young wave data ($4.3 < c_p/u_{*a} < 7.4$) obtained by TEA96 and the more developed sea conditions ($13.5 < c_p/u_{*a} < 28.6$) measured by DDTK96.

Here F is defined as the integral of the wave growth rate function γ over the wave spectrum $S_{\eta\eta}$

$$F = \frac{g\rho_a}{\rho_w}\int \omega\gamma(\omega)S_{\eta\eta}(\omega)\,d\omega, \tag{5}$$

where ρ_a and ρ_w are the densities of air and water, respectively, g is gravity, and ω is the radian frequency (TEA96). We used the growth rate function γ of Donelan et al. (2006), which was derived from direct field measurements of the wave-induced pressure in airflow over water waves. The formulation where the wind forcing was parameterized in terms of U_{10} was employed (see Jones 2007).

To compare the Grizzly Bay ε measurements with the TEA96 scaling, we identified and removed ε measurements that scaled with the surface wind stress log-layer [Eq. (2)] or the bed stress log-layer [Eq. (3)] such

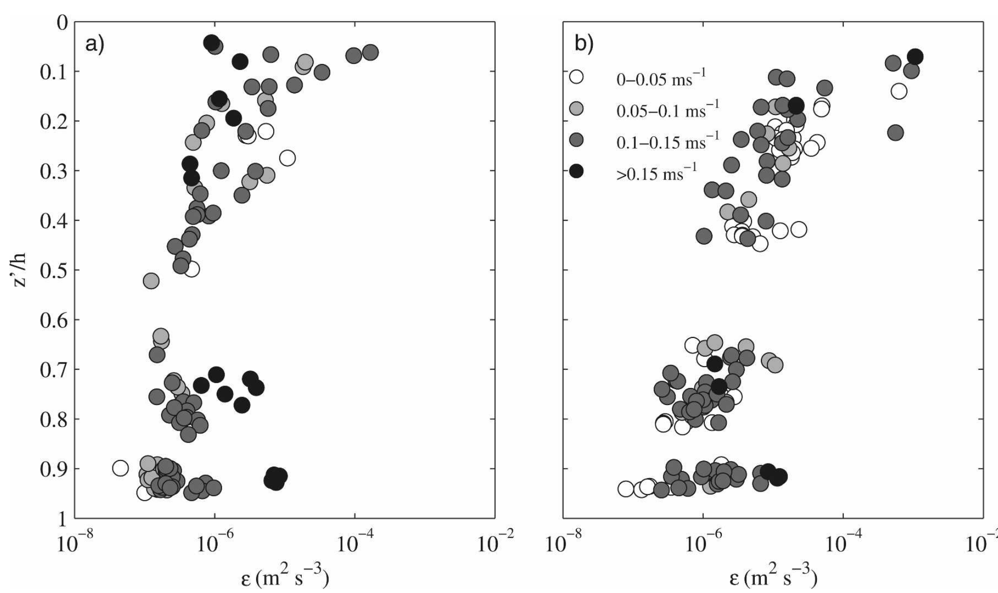

FIG. 9. Vertical profiles of the dissipation of TKE over the normalized depth for (a) weak (0–4 m s^{-1}) and (b) strong (8–10 m s^{-1}) wind velocity. The magnitude of the depth-averaged water velocity is distinguished by the shade of the data point.

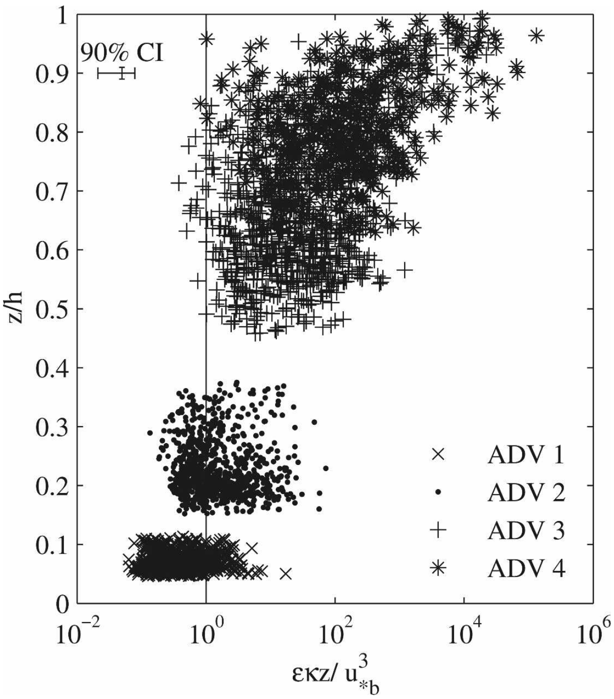

FIG. 10. Dissipation normalized using bed boundary layer scaling, assuming turbulent production of TKE via the bed stress. The vertical line is the prediction from wall-layer theory.

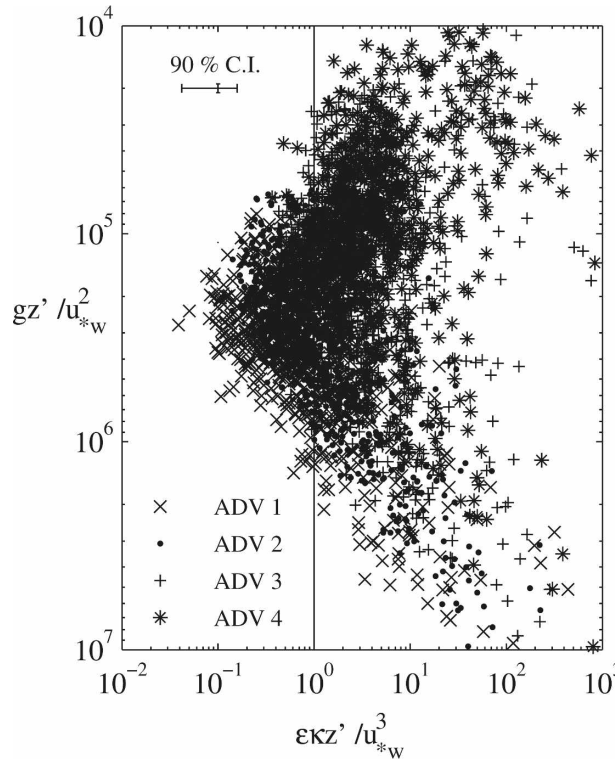

FIG. 11. As in Fig. 10, but for wind-driven surface boundary layer scaling, assuming TKE production via the wind stress.

that the remaining data were assumed to be from the transition layer. No measurements were made above the trough of the largest wave; therefore, the region of direct injection of turbulence by the whitecapping waves was not resolved. The remaining data (161 measurements) are plotted in Fig. 12, scaled as $\varepsilon H_s/F$, along with the WAVES (TEA96) and Surface Wave Dynamics Experiment (SWADE) (DDTK96) datasets. The best-fit line to the WAVES and SWADE datasets [Eq. (1)] approximates the Grizzly Bay data quite well. A least squares fit reveals that the Grizzly Bay data is best described by $c = 0.20 \pm 0.05$ and $b = 2.2 \pm 0.25$, where the uncertainty in b and c are at the 95% confidence level ($r^2 = 0.71$): b is in good agreement with the best fit of the WAVES and SWADE datasets; however, c is slightly smaller than that derived from the WAVES and SWADE datasets.

The use of H_s as the scale for depth was chosen by TEA96 as it has been associated with the depth of turbulent energy penetration due to wave breaking (Rapp and Melville 1990). However, an alternative length scale is the inverse of the peak wavenumber k_p (DDTK96). We note that H_s and k_p are not independent quantities when wave steepness is limited by breaking. Fits to the SWADE (DDTK96) and WAVES (TEA96) datasets by DDTK96 indicate that

$$\frac{\varepsilon}{k_p F} = d(z' k_p)^{-g}, \tag{6}$$

with $d = 0.1$ and $g = 2$. The data presented in Fig. 12a are plotted again in Fig. 12b with the length scale ${k_p}^{-1}$. For this scaling, the best fit to the Grizzly Bay data gives $d = 0.04 \pm 0.01$ and $g = 2.2 \pm 0.2$ ($r^2 = 0.70$).

5. Initiation of whitecapping

Knowledge of the conditions under which whitecapping is initiated is central to the prediction of the dynamics resulting from an applied wind stress. The probability of wave breaking in finite-depth water is a function of both the wave steepness and the relative height of the wave compared to the water depth (Babanin et al. 2001).

The contribution of depth-limited bottom interaction to wave breaking can be assessed by considering the equation that describes the asymptotic depth limit for both the nondimensional energy, $E^* = g^2E/U_{10}^4$ and the nondimensional wavenumber, $k^* = k_pU_{10}^2/g$, as a function of the nondimensional depth, $\delta = gh/U_{10}^2$, (Young and Verhagen 1996; Young and Babanin 2006). By identifying Grizzly Bay data within 20% of the asymp-

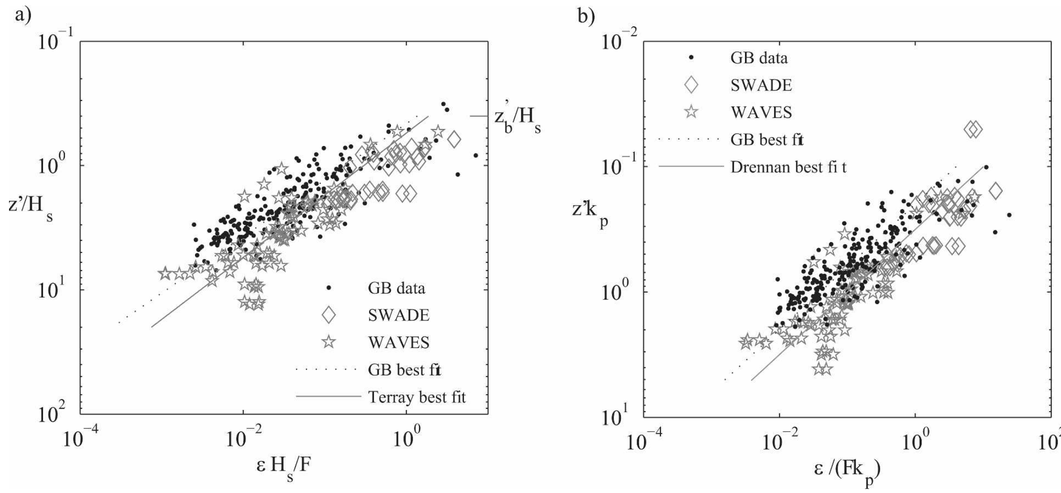

FIG. 12. Dissipation normalized (a) using TEA96 scaling, where z_b is the length scale of the breaking zone, and (b) using DDTK96 k_p scaling. The SWADE and WAVES datasets and the best-fit line are shown for comparison.

totic depth-limit equations as depth limited, we estimated that the waves were depth limited between 6% and 13% of the observation period. This indicates that depth-limited bottom interaction was not contributing greatly to wave breaking during the Grizzly Bay field study.

At the beginning of every hour during daylight five photographs were taken, resulting in 1835 total images for 367 different conditions. We noted the presence or absence of whitecapping for each of the images. The percentage of images with whitecapping, images without whitecapping, and unidentifiable images as a function of the wave age, wind speed, and significant spectral peak steepness is shown in Fig. 13. The significant spectral peak steepness ξ of the wave field is a direct measure of the nonlinearity of the dominant waves and is therefore a common parameter used to predict wave breaking (Banner et al. 2000):

$$\xi = \frac{H_p k_p}{2}, \tag{7}$$

where

$$H_p = 4\left(\int_{0.7f_p}^{1.3f_p} S_{\eta\eta}(f)\,df\right)^{1/2}.$$

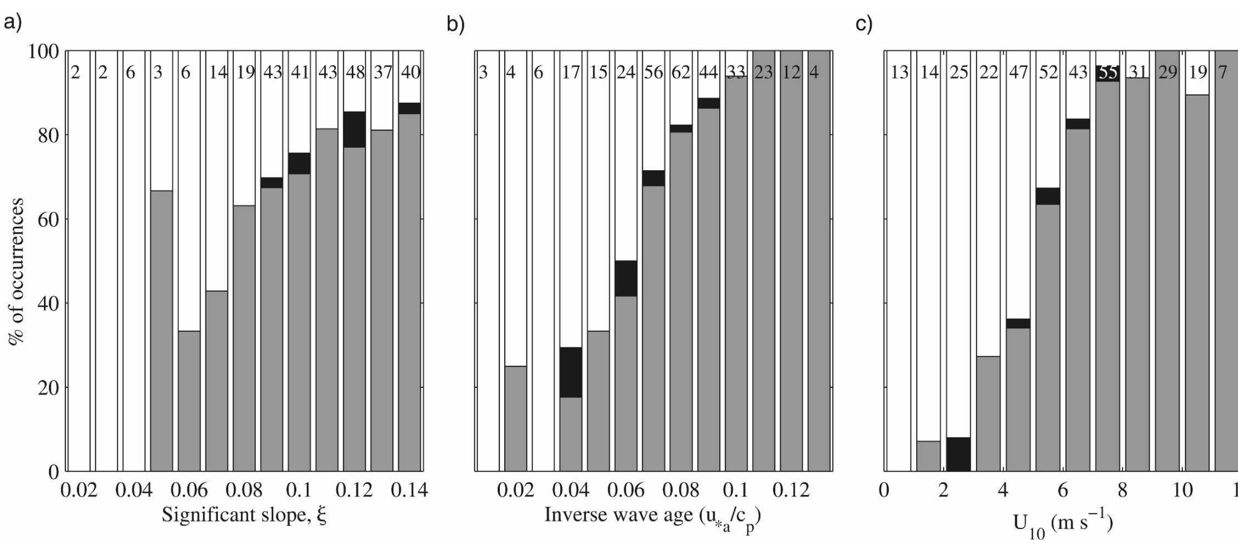

FIG. 13. Percentage of images with and without whitecapping (gray and white, respectively), as well as unidentifiable images (black), as a function of (a) significant spectral peak steepness ξ, (b) inverse wave age u_{*a}/c_p, and (c) wind velocity at 10 m U_{10}. The number of images in each bin is listed at the top of each column.

Here $S_{\eta\eta}$ is the frequency spectrum of the waves. The wave-breaking threshold value of $\xi = 0.05$, previously found for deep (Banner et al. 2000) and finite-depth (Babanin et al. 2001) water conditions, appears to hold for the Grizzly Bay conditions (Fig. 13a). In the Grizzly Bay experiment, ξ exceeded the threshold value during 90% of the observation periods, indicating that wave breaking was likely to occur mostly due to the nonlinearity of the waves. The shear in the mean current, owing to the tide and wind stress, may have led to a reduced local wave slope at breaking (Banner and Tian 1998); however, insufficient samples under conditions of low ξ were available to determine if a difference in the threshold of ξ resulted when the tide opposed or followed the wave direction.

At an inverse wave age of 0.06, approximately 50% of the time the sea state was identified as whitecapping (Fig. 13b). As expected, younger waves, that is, above an inverse wave age of 0.06, exhibited greater occurrences of whitecapping, and more fully developed waves exhibited whitecapping for a smaller fraction of the observations. In agreement with the deep water observations of Stips et al. (2005), whitecapping was absent for $U_{10} < 3$ m s^{-1} (Fig. 13c). However, U_{10} had to increase to 5 m s^{-1} before greater than 50% of the observations indicated whitecapping conditions. Other studies have reported U_{10} thresholds as low as 2 m s^{-1} (e.g., Thorpe 1982).

6. Rate of energy input to waves

A number of one-dimensional vertical models have been developed that attempt to capture the effects of surface wave breaking (e.g., Craig and Banner 1994; Burchard 2001; Umlauf et al. 2003; Feddersen and Trowbridge 2005; Jones and Monismith 2008). Common to all of these models is the parameterization of the flux of TKE at the surface that is used to simulate the effects of wave breaking. Following Kundu (1980), the surface TKE flux is parameterized as $F_b = \alpha u_{*w}^3$, where α is referred to as the wave energy parameter and is argued to be dependent on the wave age (e.g., DDTK96; TEA96). Craig and Banner (1994) selected $\alpha = 100$ and many modeling studies have followed this choice (e.g., Burchard 2001; Stips et al. 2005). If the surface TKE flux is estimated to be equal to the wind input, Eq. (5), then $F \approx F_b = \alpha u_{*w}^3$. Using this assumption, Wang and Huang (2004) found that $\alpha = 80$ best fit the SWADE and WAVES datasets, showing that α was relatively insensitive to wave ages varying between 7.4 and 28.6. To compare the appropriate choice of α for different conditions, Feddersen et al. (2007) assumed the TEA96 form to hold, [Eq. (1) with $c = 0.3$, $b = 2$] and, by regression, found $\alpha = 250$ to best fit their nearshore dataset. For the Grizzly Bay conditions, least squares regression of the calculated F and u_{*w} revealed that the relationship $F \propto u_{*w}^3$ holds (Fig. 14). Assuming $F = \alpha u_{*w}^3$ resulted in $\alpha = 54 \pm 6$ (at the 95% confidence level).

Although the estimate of α is similar to that derived from the WAVES and SWADE datasets (Fig. 14), the smaller value of α may be due to the conditions found in Grizzly Bay. The wave ages experienced during this experiment are within the range measured in the SWADE and WAVES experiments; therefore, wave age does not explain the difference in α. Processes such as the refraction of the waves in the bay that leads to the wind and wave directions not being aligned may account for the smaller wave energy parameter α; that is, less wind energy may be transferred to the waves when they are not aligned with the wind direction. The photograph time series revealed that the development of Langmuir circulation accompanied whitecapping waves at this field location. Smith (1999) speculated that Langmuir circulation might account for the variation in the magnitude of α among different locations.

7. Transition depth

Depending on the relative strength of the three possible factors influencing the distribution of TKE (the wind stress, whitecapping waves, and bed stress), four different scenarios for the distribution of TKE are possible (in the absence of buoyancy forcing). The scaling arguments used to describe the different layers [Eqs. (1)–(3)] can be used to estimate the position of transition between the layers (Fig. 15). In the absence of wind, and therefore whitecapping waves, the bottom log-layer develops until it extends from the bed to the surface with ε decreasing away from the bed as production decreases. Under light wind conditions, that is, before the onset of waves, the wind-induced boundary layer will overlap with the BBL. Higher values of ε will occur close to the bed and close to the water surface where shear production is high. Shear production and ε will remain in balance over the water column; therefore, the transition from the dominant production of TKE by the wind stress log-layer to the bed stress log-layer will be determined by the relative size of the bed stress to the surface stress. To define the height of this transition we equate Eqs. (2) and (3):

$$z_{t1} = \frac{h}{u_{*w}^3/u_{*b}^3 + 1}. \tag{8}$$

In the limit $u_{*w} \ll u_{*b}$, z_{t1} approaches h; conversely, if $u_{*w} \gg u_{*b}$, z_{t1} approaches zero.

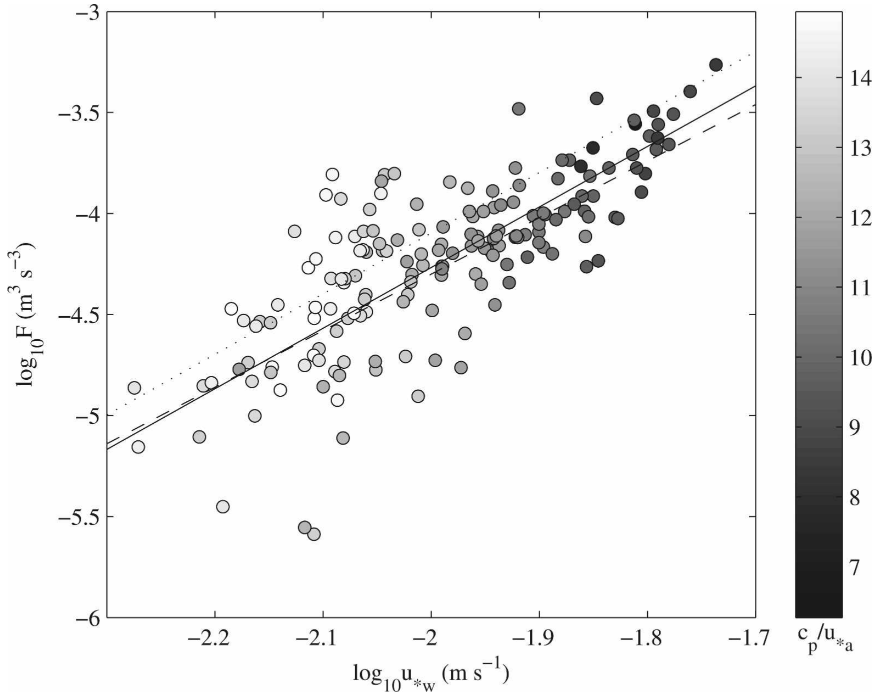

FIG. 14. Parameterization of the wind energy input to the waves F as a function of the surface stress u_{*w}, observations (circles, the grayscale indicates the wave age), line of best-fit $20u_{*w}^{2.8}$ (dashed line), $54u_{*w}^3$ (solid line), and $80u_{*w}^3$ (dotted line).

The third possible scenario is the existence of three distinct layers. When the wind velocity increases sufficiently to produce waves, the WASL appears [described by Eq. (1)] and the wind stress log-layer may exist between the WASL and the tidal BBL (Fig. 15). We defined the transition between the WASL and the wind-driven log-layer by equating Eq. (1) (with $b = 2$ and $c = 0.2$) and Eq. (2) and assuming $F = \alpha u_{*w}^3$:

$$z_{t2} = h - 0.2H_s\kappa\alpha. \tag{9}$$

Finally, the fourth possible scenario is the direct transition of the WASL to the BBL; that is, the wind stress log-layer does not exist. We estimated the location of the transition between the two layers by equating Eqs. (1) and (3), resulting in the transition to breaking-wave-dominated ε being defined as a height above the bed:

$$z_{t3} = \left[-\left(0.2\alpha\kappa H_s \frac{u_{*w}^3}{u_{*b}^3} + 2h\right) + \sqrt{\left(0.2\alpha\kappa H_s \frac{u_{*w}^3}{u_{*b}^3} + 2h\right)^2 - 4h^2} \right] / (-2). \tag{10}$$

We note that the influence of the suspended sediment stratification is not included in the calculation of the theoretical transition depths.

As discrete measurements of ε were made throughout the water column, it was not possible to identify the transition points between the different layers in the water column (as identified by the dominant source of TKE). However, we compared each of the ε measurements with Eqs. (1)–(3) so as to identify whether each measurement was in the bed stress log-layer, the wind stress log-layer, or the transition layer, respectively (Fig. 16). Observations of ε in the bottom 10% of the water column were not included in this analysis owing to the influence of suspended sediment stratification (see section 4a). The transition heights between the wind stress log-layer and the bed stress log-layer z_{t1} [Eq. (8)] and the transition heights between the WASL and bed stress log-layer z_{t3} [Eq. (10)] are shown for the range of conditions experienced during the field experiment (Fig. 16). Since H_s is a function of both h and u_{*w}, the contours showing z_{t3} for different wave conditions are specific to the Grizzly Bay wave conditions.

When the wind stress u_{*w} was smaller than the bed stress u_{*b}, shear production due to the bed stress was the dominant source of TKE, and most of the measurements below the z_{t1} line were identified as scaling with

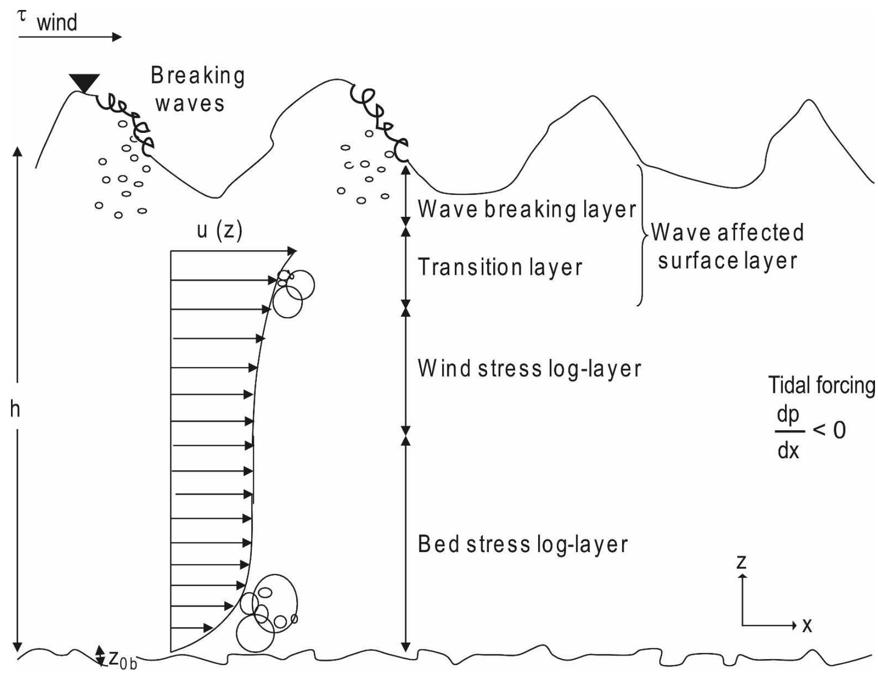

FIG. 15. Schematic overview of the vertical structure of a shallow water column resulting from the combined forcing of wind stress and tide pressure gradient (from Jones and Monismith 2008).

the bed stress. As the wind stress increases, the wave height can also increase and the normalized depth of the WASL z_{t3} increases accordingly. For $u_{*w}/u_{*b} > 1$, the majority of the observations in the upper water column ($z/h > 0.5$) were identified as scaling with the WASL. We identified a small number of observations as scaling with the wind stress log-layer. Closer to the bed ($0.15 < z/h < 0.3$), observations were classified as scaling with the WASL or the bed stress log-layer. The collocation of observations that scaled with the transition layer and the bed stress log-layer was anticipated since the transition depth z_{t3} is a function of H_s (see dashed lines in Fig. 16).

Equations (8)–(10) can be used to predict which of the four possible scenarios best describes the vertical structure as well as predict the heights of transitions between the layers for the conditions measured during the experiment. For example, to determine the depth of influence of the WASL we need to first determine if a wind-driven log-layer will exist ($z_{t2} > z_{t3}$) or if the WASL transitions directly to the tidal boundary layer ($z_{t2} < z_{t3}$).

For the subset of cases where the water column was well mixed, which included 86% of the observations, all of the cases were identified as producing a WASL that transitions directly to a bed stress log-layer. Figure 17 illustrates that under whitecapping conditions, 50% of the time whitecapping waves provided the dominant source of TKE over 90% (or more) of the water column. Whitecapping waves provide the dominant source of TKE over 50% or less of the water column for only 10% of the conditions.

8. Discussion

A smaller value of c was found to best describe the WASL for the Grizzly Bay dataset ($c = 0.2$), compared with the deep water result of the WAVES and SWADE experiments ($c = 0.3$). The different growth rate functions employed in this study and the TEA96 study did not account for this difference. TEA96 employed the Donelan and Pierson (1987) algorithm for estimating the growth rate function γ. Applying the Donelan and Pierson algorithm for γ to the Grizzly Bay dataset led to larger estimates of F on average than the Donelan et al. (2006) algorithm. Fits to Eqs. (1) and (6) were repeated for the dataset using the Donelan and Pierson algorithm for γ, resulting in $c = 0.16 \pm 0.02$, $b = 2.4 \pm 0.2$ ($r^2 = 0.69$), $d = 0.03 \pm 0.01$, and $g = 2.3 \pm 0.14$ ($r^2 = 0.69$). Furthermore, comparison of F [derived using the Donelan and Pierson algorithm for γ] with u_{*w}^3 led to $\alpha = 61 \pm 5$. This demonstrates that the parameterization of ε and F are relatively insensitive to the choice of the growth rate algorithm.

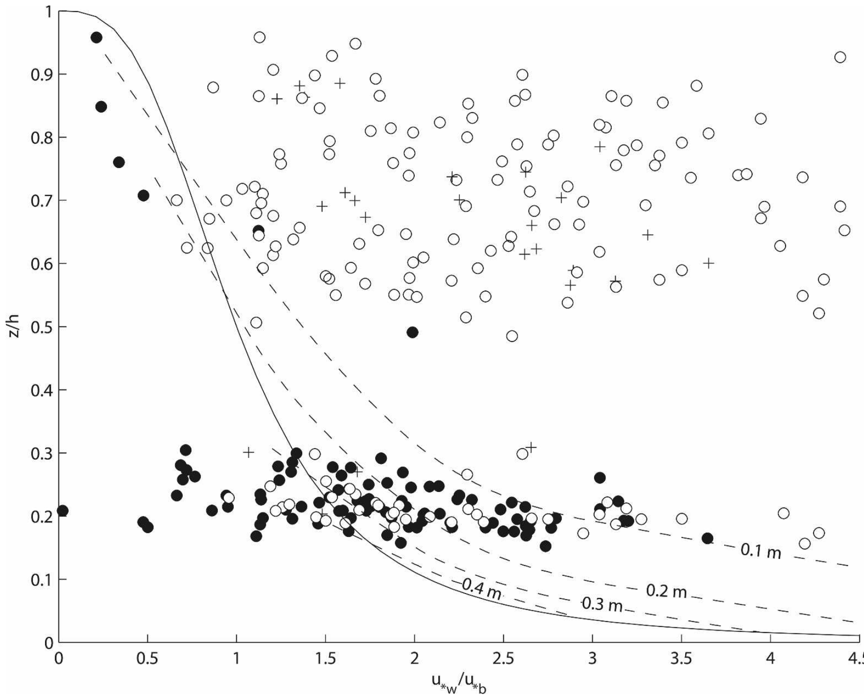

FIG. 16. Height above the bed z normalized by the total water depth h vs proportion of wind stress to bed stress u_{*w}/u_{*b}. Dissipation measurements are classified according to the scaling that most appropriately describes their magnitude: the bed stress log-layer [Eq. (3), black circles], wind stress log-layer [Eq. (2), crosses] or whitecapping surface layer [Eq. (1), open circles]. Theoretical transition depths are shown for the wind stress log-layer to bed stress log-layer z_{t1} [Eq. (8), black line] and the transition from the whitecapping surface layer to the bed stress log-layer z_{t3} for different wave heights [Eq. (10), dashed lines] for conditions experienced during the Grizzly Bay experiment.

The TEA96 deep water wave breaking scaling assumes that the flux of energy from wave breaking into the water column is approximately equal to the energy input from the wind to the waves. This assumption requires that only a small portion of the wind energy be retained by the waves for wave growth. The smaller values of c and d estimated from the Grizzly Bay measurements compared with the WAVES and SWADE measurements may be the result of a smaller conversion of the wind energy to wave breaking under the Grizzly Bay conditions. This could be the result of wave growth using a larger portion of the wind energy flux at this site. The difference in c demonstrates that care must be taken in extending the results of the Grizzly Bay measurements to other locations and conditions.

Alternatively, the difference in the magnitude of c may be the result of a different depth of the wave-breaking layer. The TEA96 model of the WASL purports that it consists of the wave breaking layer followed by the transition layer described by Eq. (1), where the transition occurs at depth z'_b, known as the breaking depth. TEA96 described the breaking depth

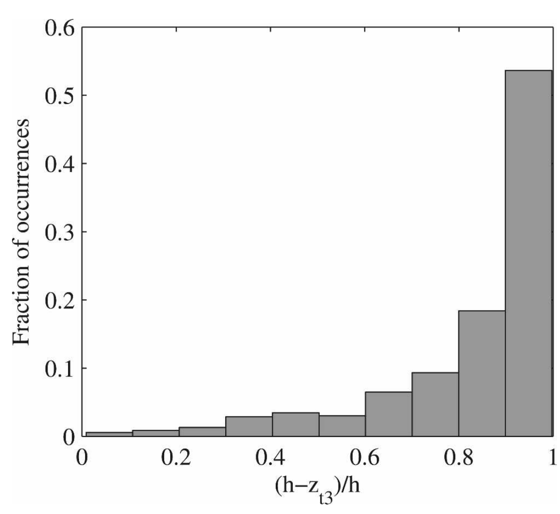

FIG. 17. Distribution of normalized transition depth between the layer where the dominant source of TKE is whitecapping to the bed stress log-layer $(h - z_{t3})/h$: $(h - z_{t3})/h = 0$ indicates that the bed stress log-layer extends to the surface and $(h - z_{t3})/h = 1$ indicates that whitecapping is the dominant source of TKE over the entire water column.

as the maximum depth of direct injection of energy by the waves. Stationary instrument experiments do not allow measurement of ε above the wave troughs; therefore, z_b was estimated by TEA96 by assuming 1) that the total energy dissipated in the water column (owing to wind energy input) is equal to the integral of ε over the WASL and 2) that the magnitude of the wave breaking layer is equal to the value of ε at the top of the transition layer; that is,

$$\varepsilon = \frac{0.2F}{H_s}\left(\frac{z'_b}{H_s}\right)^{-2.2} \quad \text{for} \quad z' < z'_b. \tag{11}$$

In section 7 it was shown that, in the presence of whitecapping waves, the WASL overlapped with the bed stress log-layer at a height above the bed defined by Eq. (10). Assuming that we can neglect direct viscous stresses on the surface, the production of kinetic energy in the water column by shear currents and losses due to bed friction, z_b can be found by assuming the total energy dissipated in the water column (due to wind energy input) is equal to the integral of ε over the WASL, as modeled by Eqs. (1) and (11). We note that ε due to tidal forcing is not included in this integral. Assuming that z'_b scales with H_s, as assumed for the deep water wave breaking case (TEA96), it can be shown that $z'_b = 0.4H_s$. This is between $z'_b = 0.25H_s$, found by Young and Babanin (2006a), and $z'_b = 0.6H_s$, found to best describe the TEA96 dataset. According to the TEA96 model, the distribution of ε throughout the water column for the Grizzly Bay experiment is described

$$\varepsilon = \begin{cases} \dfrac{0.2F}{H_s}(0.4)^{-2.2} & \text{for} \quad 0 < z' < 0.4H_s \\[2ex] \dfrac{0.2F}{H_s}\left(\dfrac{z'}{H_s}\right)^{-2.2} & \text{for} \quad 0.4H_s < z' < h - z_{t3} \\[2ex] \dfrac{u_{*b}^3}{\kappa(h - z')} & \text{for} \quad h - z_{t3} < z' < h. \end{cases} \tag{12}$$

The concept of a constant-dissipation layer that scales with H_s has been challenged by the recent wave-following measurements of Soloviev and Lukas (2003) and Gemmrich and Farmer (1999 2004) where measurements were made above the wave troughs.

Assuming wave growth to be minimal, TEA96 assumed that for deep water, the vertical integral of ε in the water column (due to wind energy input) was equal to F. In finite-depth water an additional term is present, the energy dissipation owing to friction in the wave boundary layer. For a monochromatic wave, the time-averaged rate of energy dissipation is (Jonsson 1966)

$$E_B = \frac{2}{3\pi} f_e U_{\max}^3, \tag{13}$$

where $U_{\max}$ is the maximum horizontal wave orbital velocity at the bed and f_e is the energy dissipation factor. The range of relative roughness (A_b/k_s) and bottom amplitude Reynolds number ($\mathrm{Re}_b = A_b U_{\max}/\nu$) indicates that the wave boundary layer is laminar throughout the experiment, where the excursion length is $A_b = U_{\max}/\omega$. Therefore, the wave friction factor is (Jonsson 1966)

$$f_e = \frac{3\sqrt{2}\pi}{8\sqrt{\mathrm{Re}_b}}. \tag{14}$$

To extend these equations to spectral waves, Mirfenderesk and Young (2003) found that $U_{\max}$ in Eq. (13) should be replaced by $1.88U_{\mathrm{rms}}$, where U_{rms} is the root-mean-square velocity at the bed and the frequency should equal the peak frequency. Throughout the Grizzly Bay experiment, U_{rms} ranged from 0 to 0.16 m s^{-1} and E_B, a small fraction of the total wind energy input throughout the month-long experiment, ranged from $1 \times 10^{-6.5}$ to $1 \times 10^{-4.5}$ m^3 s^{-3}. During the majority of the measurements the proportion of energy lost at the bed was less than 10% of F. The maximum proportion of energy lost at the bed was roughly 20%.

As noted in section 5, Langmuir circulations accompanied whitecapping waves at the measurement site. Langmuir circulations can potentially provide a significant source of TKE production at the surface, $P_{\mathrm{LC}} = u_s u_{*w}^2$, where u_s is the magnitude of the Stokes drift at the water surface (Skyllingstad and Denbo 1995). The ratio of the TKE flux owing to Langmuir circulations to the TKE flux due to whitecapping waves (αu_{*w}^3) is therefore $u_s/\alpha u_{*w}$. For the conditions experienced in the Grizzly Bay experiment, the TKE flux owing to Langmuir circulation is expected to be less than 10% of the surface TKE flux due to whitecapping for 90% of the measurements. For the remaining 10% of conditions, the ratio did not exceed 20%. Therefore, we conclude that during conditions of whitecapping waves, the dominant TKE flux at the water surface is due to the whitecapping waves. However, we note that Langmuir cells may contribute to enhanced ε at depth by vertically transporting wave-breaking-generated turbulence (Nepf et al. 1995). Furthermore, we note that due to a lack of observations during low wind speed, nonwhitecapping conditions the contribution of small-scale Langmuir circulation to near-surface turbulence could not be evaluated (Veron and Melville 2001).

9. Summary and conclusions

The TKE dissipation rate in a wind- and tide-forced shallow embayment was studied. The dataset demonstrated that whitecapping surface waves can influence the distribution and magnitude of TKE in the water column. Generation of whitecapping waves occurred for significant spectral peak steepness greater than 0.05 or above a wind speed of approximately 3 m s^{-1}. The probability of the occurrence of whitecapping reached 50% for wind speeds greater than 5 m s^{-1}.

The data demonstrated that the tide- and wind-forced shallow water column was best described by a two-layer structure in which the layers are termed the wave-affected surface layer and the bed stress log-layer. Measurements in the WASL show that ε decays as $z'^{-2.2}$, roughly following the deep water wave breaking scaling developed by TEA96. In the bed stress log-layer, shear production due to the tide pressure gradient was the dominant source of TKE. The scaling relationships were used to derive a relationship to predict the depth of transition between the bed stress log-layer and the WASL; this depth was shown to be dependent on the size of u_{*w} relative to u_{*b} as well as H_s [Eq. (10)]. For 50% of the month-long experiment the WASL extended over 90% or more of the water column. Further measurements of the water surface and wave troughs are needed to elucidate the wave breaking layer.

Without the incorporation of whitecapping effects, numerical models of shallow water bodies where the BBL overlaps with the WASL will not predict the correct distribution of TKE or the correct mean current profiles, thus preventing the accurate prediction of the mixing and transport of constituents such as sediment and phytoplankton. Validation of a one-dimensional numerical model to simulate the influence of whitecapping waves in a shallow estuarine environment is presented in Jones and Monismith (2008).

Knowledge of the distribution of ε in the water column due to whitecapping is paramount to understanding and modeling the evolution of wind-generated waves in finite-depth water. As discussed by Young et al. (2005), in deep-water conditions the evolution of the wave spectrum for idealized, fetch-limited conditions is reasonably well known. However, knowledge of the whitecapping dissipation term, particularly in finite-depth conditions, is limited. These measurements can be used to improve numerical models of finite-depth wind wave dissipation.

The conditions experienced in Grizzly Bay during the month-long experiment are typical of conditions experienced for eight months of the year in San Francisco Bay. Many shallow water locations in San Francisco Bay, as well as other estuarine and coastal regions, are likely to experience conditions similar to those in Grizzly Bay; thus, it appears that wave breaking plays an important role in the dynamics of many shallow estuaries.

Acknowledgments. Thanks are due to F. Parchaso, B. Richards, and J. Thompson from the U.S. Geological Survey for assistance with the field experiment. We would also like to thank K. Davies, D. Fong, S. Giddings, J. Hench, R. Lowe, C. McDonald, N. Nidzieko, J. Rosman, U. Shavit, J. Steinbuck, and C. Troy for their help in collecting the field dataset. The authors thank J. Thompson, K. Arrigo, and F. Feddersen for comments on an earlier version of the manuscript. The manuscript benefited substantially from the comments of two anonymous reviewers. The work was generously supported by the CALFED Bay Delta Authority Environmental Restoration Program (Grant ERP02P22) and The Foundation for Young Australians Centenary Scholarship Award.

APPENDIX

Estimates of ε from Vertical Velocity Spectra

The purpose of this appendix is to present the equations used to estimate ε from the vertical velocity spectra $S_{w'w'}$ in the presence of oscillatory and mean motion as theoretically derived by Lumley and Terray (1983) and implemented by Feddersen et al. (2007). Here ε is defined as

$$\varepsilon(\omega) = \left[\frac{S_{w'w'}(\omega)(2\pi)^{3/2}}{\varsigma M_{w'w'}(\omega)}\right]^{3/2}, \qquad \text{(A1)}$$

where $\varsigma = 1.5$ is Kolmogorov's constant and $M_{lm}(\omega)$ is an integral over three-dimensional wavenumber space that depends on the mean flow and the wave orbital velocities; that is,

$$M_{lm}(\omega) = \int_{-\infty}^{\infty}\int_{-\infty}^{\infty}\int_{-\infty}^{\infty} \frac{k^{-11/3}\left(\delta_{lm} - \dfrac{k_l k_m}{k^2}\right)}{\sqrt{\sigma_i^2 k_i^2}} \times \exp\left[-\frac{(k_1\overline{u}_1 + k_2\overline{u}_2 - \omega)^2}{2\sigma_i^2 k_i^2}\right] dk_1\, dk_2\, dk_3. \qquad \text{(A2)}$$

Here $\mathbf{k} = [k_1\ k_2\ k_3]$ is the wavenumber vector with $k = |\mathbf{k}|$, $\overline{u}_i$ is the ith component of the mean velocity, and σ_i is the ith component of the variance of the wave-induced velocity. The integral in Eq. (A2) is evaluated numerically using the observed $\overline{u}_i$ and σ_i. To achieve this, two coordinate transforms are performed as detailed in Feddersen et al. (2007). The advantage of the Feddersen et al. method is that it does not assume $\sigma_2 = \sigma_3 = 0$.

REFERENCES

Agrawal, Y. C., E. A. Terray, M. A. Donelan, P. A. Hwang, A. J. Williams, W. M. Drennan, K. K. Kahma, and S. A. Kitaigorodskii, 1992: Enhanced dissipation of kinetic energy beneath surface waves. *Nature,* **359,** 219–220.

Anis, A., and J. N. Moum, 1995: Surface wave–turbulence interactions. Scaling $\varepsilon(z)$ near the sea surface. *J. Phys. Oceanogr.,* **25,** 2025–2045.

Babanin, A. V., I. R. Young, and M. L. Banner, 2001: Breaking probabilities for dominant surface waves on water of finite constant depth. *J. Geophys. Res.,* **106,** 11 659–11 676.

Banner, M. L., and X. Tian, 1998: On the determination of the onset of breaking for modulating surface gravity water waves. *J. Fluid Mech.,* **367,** 107–137.

——, A. V. Babanin, and I. R. Young, 2000: Breaking probability for dominant waves on the sea surface. *J. Phys. Oceanogr.,* **30,** 3145–3160.

Bricker, J. D., S. Inagaki, and S. G. Monismith, 2005: Bed drag coefficient variability under wind waves in a tidal estuary. *J. Hydraul. Eng.,* **131,** 497–508.

Burchard, H., 2001: Simulating the wave-enhanced layer under breaking surface waves with two-equation turbulence models. *J. Phys. Oceanogr.,* **31,** 3133–3145.

Cacchione, D., D. Drake, R. Kayen, R. Sternberg, G. Kineke, and G. Tate, 1995: Measurements in the bottom boundary-layer on the Amazon subaqueous delta. *Mar. Geol.,* **125,** 235–257.

Conomos, T. J., R. E. Smith, and J. W. Gartner, 1985: Environmental setting of San Francisco Bay. *Hydrobiologia,* **129,** 1–12.

Craig, P. D., and M. L. Banner, 1994: Modeling wave-enhanced turbulence in the ocean surface layer. *J. Phys. Oceanogr.,* **24,** 2546–2559.

Craik, A. D. D., and S. Leibovich, 1976: A rational model for Langmuir circulations. *J. Fluid Mech.,* **73,** 401–426, doi:10.1017/S0022112076001420.

Donelan, M. A., 1990: Air–sea interaction. *The Sea,* B. LeMehaute and D. M. Hanes, Eds., Vol. 9, *Ocean Engineering Science,* Wiley, 239–292.

——, and W. J. Pierson Jr., 1987: Radar scattering and equilibrium ranges in wind-generated waves with application to scatterometry. *J. Geophys. Res.,* **92,** 4971–5029.

——, A. V. Babanin, I. R. Young, and M. L. Banner, 2006: Wave-follower field measurements of the wind-input spectral function. Part II: Parameterization of the wind input. *J. Phys. Oceanogr.,* **36,** 1672–1689.

Drennan, W. M., M. A. Donelan, E. A. Terray, and K. B. Katsaros, 1996: Oceanic turbulence dissipation measurements in SWADE. *J. Phys. Oceanogr.,* **26,** 808–815.

Emery, W., and R. Thomson, 2001: *Data Analysis Methods in Physical Oceanography*. 2nd ed. Elsevier, 638 pp.

Feddersen, F., and J. H. Trowbridge, 2005: The effect of wave breaking on surf-zone turbulence and alongshore currents: A modeling study. *J. Phys. Oceanogr.,* **35,** 2187–2203.

——, and A. J. Williams III, 2007: Direct estimation of the Reynolds stress vertical structure in the nearshore. *J. Atmos. Oceanic Technol.,* **24,** 102–116.

——, J. H. Trowbridge, and A. J. Williams III, 2007: Vertical structure of dissipation in the nearshore. *J. Phys. Oceanogr.,* **37,** 1764–1777.

Gargett, A. E., 1989: Ocean turbulence. *Annu. Rev. Fluid Mech.,* **21,** 419–451.

Gemmrich, J. R., and D. M. Farmer, 1999: Near-surface turbulence and thermal structure in a wind-driven sea. *J. Phys. Oceanogr.,* **29,** 480–499.

——, and ——, 2004: Near-surface turbulence in the presence of breaking waves. *J. Phys. Oceanogr.,* **34,** 1067–1086.

Green, M. O., and I. N. McCave, 1995: Seabed drag coefficient under tidal currents in the eastern Irish Sea. *J. Geophys. Res.,* **100,** 16 057–16 069.

Greenan, B. J. W., N. S. Oakey, and F. W. Dobson, 2001: Estimates of dissipation in the ocean mixed layer using a quasi-horizontal microstructure profiler. *J. Phys. Oceanogr.,* **31,** 992–1004.

Gross, T. F., and A. R. M. Nowell, 1985: Spectral scaling in a tidal boundary layer. *J. Phys. Oceanogr.,* **15,** 496–508.

Heathershaw, A. D., 1979: Turbulent structure of the bottom boundary layer in a tidal current. *Geophys. J. Int.,* **58,** 395–430.

Isobe, M., K. Kondo, and K. Horikawa, 1984: Extension of MLM for estimating directional wave spectrum. *Proc. Symp. on Description and Modeling of Directional Seas,* Paper A-6, Copenhagen, Denmark, Danish Hydraulic Institute, 1–15.

Johnson, D., 2002: DIWASP, a directional wave spectra toolbox for MATLAB: User manual. Centre for Water Research, University of Western Australia, Research Rep. WP-1601-DJ (V1.1), 19 pp. [Available online at http://www.metocean.co.nz/webcontent/software/DIWASP_manual.pdf.]

Jones, N. L., 2007: The role of wind waves and currents on vertical mixing in shallow water bodies: Implications for phytoplankton distribution. Ph.D. dissertation, Stanford University, 209 pp.

——, and S. G. Monismith, 2007: Measuring short-period wind waves in a tidally forced environment with a subsurface pressure gauge. *Limnol. Oceanogr. Methods,* **5,** 317–327.

——, and ——, 2008: Modeling the influence of wave-enhanced turbulence in a shallow tide- and wind-driven water column. *J. Geophys. Res.,* **113,** C03009, doi:10.1029/2007JC004246.

Jonsson, I. G., 1966: Wave boundary layers and friction factors. *Proc. 10th Int. Conf. on Coastal Engineering,* Tokyo, Japan, ASCE, 127–148.

Kranck, K., and T. G. Milligan, 1992: Characteristics of suspended particles at an 11-hour anchor station in San Francisco Bay, California. *J. Geophys. Res.,* **97,** 11 373–11 382.

Kundu, P. K., 1980: A numerical investigation of mixed-layer dynamics. *J. Phys. Oceanogr.,* **10,** 220–236.

Lumley, J. L., and E. A. Terray, 1983: Kinematics of turbulence convected by a random wave field. *J. Phys. Oceanogr.,* **13,** 2000–2007.

Magnaudet, J., and L. Thais, 1995: Orbital rotational motion and turbulence below laboratory wind water waves. *J. Geophys. Res.,* **100,** 757–771.

Mirfenderesk, H., and I. R. Young, 2003: Direct measurements of the bottom friction factor beneath surface gravity waves. *Appl. Ocean Res.,* **25,** 269–287.

Monismith, S. G., and J. Magnaudet, 1998: On wavy mean flows, Langmuir cells, strain, and turbulence. *Physical Processes in*

Lakes and Oceans, J. Imberger, Ed., Coastal and Estuarine Studies Series, Vol. 54, Amer. Geophys. Union, 101–110.

Nepf, H. M., E. A. Cowen, S. J. Kimmel, and S. G. Monismith, 1995: Longitudinal vortices beneath breaking waves. *J. Geophys. Res.,* **100,** 16 211–16 222.

Rapp, R. J., and W. K. Melville, 1990: Laboratory measurements of deep-water breaking waves. *Philos. Trans. Roy. Soc. London,* **331A,** 735–800.

Reidenbach, M. A., S. G. Monismith, J. R. Koseff, G. Yahel, and A. Genin, 2006: Boundary layer turbulence and flow structure over a fringing coral reef. *Limnol. Oceanogr.,* **51,** 1956–1968.

Shaw, W., and J. Trowbridge, 2001: The direct estimation of near-bottom turbulent fluxes in the presence of energetic wave motions. *J. Atmos. Oceanic Technol.,* **18,** 1540–1557.

Skyllingstad, E. D., and D. W. Denbo, 1995: An ocean large-eddy simulation of Langmuir circulations and convection in the surface mixed layer. *J. Geophys. Res.,* **100,** 8501–8522.

Smith, J. A., 1999: Observations of wind, waves, and the mixed layer: The scaling of surface motion. *The Wind-Driven Air–Sea Interface: Electromagnetic and Acoustic Sensing, Wave Dynamics, and Turbulent Fluxes,* M. L. Banner, Ed., University of New South Wales, 231–238.

Soloviev, A., and R. Lukas, 2003: Observation of wave-enhanced turbulence in the near-surface layer of the ocean during TOGA COARE. *Deep-Sea Res. I,* **50,** 371–395.

Stips, A., H. Burchard, K. Bolding, H. Prandke, A. Simon, and A. Wüest, 2005: Measurement and simulation of viscous dissipation in the wave affected surface layer. *Deep-Sea Res. II,* **52,** 1133–1155.

Teixeira, M. A. C., and S. E. Belcher, 2002: On the distortion of turbulence by a progressive surface wave. *J. Fluid Mech.,* **458,** 229–267.

Terray, E. A., M. A. Donelan, Y. C. Agrawal, W. M. Drennan, K. K. Kahma, A. J. Williams, P. A. Hwang, and S. A. Kitaigorodskii, 1996: Estimates of kinetic energy dissipation under breaking waves. *J. Phys. Oceanogr.,* **26,** 792–807.

——, W. M. Drennan, and M. A. Donelan, 1999: The vertical structure of shear and dissipation in the ocean surface layer. *Proc. Symp. on the Wind-Driven Air–Sea Interface: Electromagnetic and Acoustic Sensing, Wave-Dynamics, and Turbulent Fluxes,* Sydney, Australia, University of New South Wales, 239–245.

Thompson, J. K., J. R. Koseff, S. G. Monismith, and L. V. Lucas, 2008: Shallow water processes govern system-wide phytoplankton bloom dynamics: A field study. *J. Mar. Syst.,* doi:10.1016/j.jmarsys.2007.12.006.

Thorpe, S. A., 1982: On the clouds of bubbles formed by breaking wind-waves in deep water, and their role in air–sea gas transfer. *Philos. Trans. Roy. Soc. London,* **304A,** 155–210.

——, 2004: Recent developments in the study of ocean turbulence. *Annu. Rev. Earth Planet. Sci.,* **32,** 91–109.

Trowbridge, J., 1998: On a technique for measurement of turbulent shear stress in the presence of surface waves. *J. Atmos. Oceanic Technol.,* **15,** 290–298.

——, and S. Elgar, 2001: Turbulence measurements in the surf zone. *J. Phys. Oceanogr.,* **31,** 2403–2417.

Umlauf, L., H. Burchard, and K. Hutter, 2003: Extending the k-ω turbulence model towards oceanic applications. *Ocean Modell.,* **5,** 195–218.

Veron, F., and W. K. Melville, 2001: Experiments on the stability and transition of wind-driven water surfaces. *J. Fluid Mech.,* **446,** 25–65.

Wang, W., and R. X. Huang, 2004: Wind energy input to the surface waves. *J. Phys. Oceanogr.,* **34,** 1276–1280.

Warner, J. C., D. H. Schoellhamer, C. A. Ruhl, and J. R. Burau, 2004: Floodtide pulses after low tides in shallow subembayments adjacent to deep channels. *Estuarine Coastal Shelf Sci.,* **60,** 213–228.

Young, I. R., and L. A. Verhagen, 1996: The growth of fetch limited waves in water of finite depth. 1. Total energy and peak frequency. *Coastal Eng.,* **29,** 47–78.

——, and A. V. Babanin, 2006a: The form of the asymptotic depth-limited wind wave frequency spectrum. *J. Geophys. Res.,* **111,** C06031, doi:10.1029/2005JC003398.

——, and ——, 2006b: Spectral distribution of energy dissipation of wind-generated waves due to dominant wave breaking. *J. Phys. Oceanogr.,* **36,** 376–394.

——, M. L. Banner, M. A. Donelan, A. V. Babanin, W. K. Melville, F. Veron, and C. McCormick, 2005: An integrated system for the study of wind-wave source terms in finite-depth water. *J. Atmos. Oceanic Technol.,* **22,** 814–831.